

1 **Phytoplankton dynamics driven by vertical nutrient fluxes during the spring**
2 **inter-monsoon period in the northeastern South China Sea**

3

4 Qian P. Li^{*}, Yuan Dong, Yanjun Wang

5 South China Sea Institute of Oceanology, Chinese Academy of Sciences, Guangzhou,
6 China

7

8

9 Submitted to Biogeosciences on March 27, 2015

10 Revised July 29, 2015

11 2nd revised October 5, 2015

12 3rd revised November 11, 2015

13

14 *Correspondence to: qianli@scsio.ac.cn

15 **Abstract**

16 A field survey from the coastal ocean zones to the offshore pelagic zones of the
17 northeastern South China Sea (nSCS) was conducted during the inter-monsoon period of
18 May 2014 when the region was characterized by prevailing low-nutrient conditions.
19 Comprehensive field measurements were made for not only hydrographic and
20 biogeochemical properties but also phytoplankton growth and microzooplankton grazing
21 rates. We also performed estimations of the vertical turbulent diffusivity and diffusive
22 nutrient fluxes using a Thorpe-scale method and the upwelling nutrient fluxes by Ekman
23 pumping using satellite-derived wind stress curl. Our results revealed a positive
24 correlation between the integrated phytoplankton chlorophyll-*a* and vertical nutrient
25 fluxes in the offshore region of the nSCS during the study period. We found a generally
26 increasing role of turbulent diffusion but decreasing role of curl-driven upwelling on
27 vertical transport of nutrients from the coastal ocean zones to the offshore pelagic zones
28 in the nSCS. Elevated nutrient fluxes near Dongsha Islands supported high new
29 production leading to net growth of phytoplankton community, whereas the low nutrient
30 fluxes near southwest Taiwan had resulted in a negative net community growth leading to
31 decline of a surface phytoplankton bloom. Overall, phytoplankton dynamics in the large
32 part of the nSCS are largely driven by vertical nutrient fluxes including turbulent
33 diffusion and curl-driven upwelling during the spring inter-monsoon period.

34

35

36 1. Introduction

37 Nutrient fluxes from below the euphotic zone are essential for phytoplankton primary
38 production in the surface ocean (Eppley and Peterson, 1979), while the mechanisms
39 regulating those fluxes are still inadequately understood in the northeastern South China
40 Sea (nSCS), particularly during the spring intermonsoon period. Wind-driven coastal
41 upwelling, river discharge, and inter-shelf nutrient transport were important mechanisms
42 supplying nutrients to the euphotic zone of the nSCS (Liu et al., 2002; Gan et al., 2010;
43 Han et al., 2013), while their contributions to primary production were mostly limited to
44 coastal regions as these nutrients would be mostly utilized in the coastal waters before
45 reaching the large area of the nSCS. Kuroshio intrusion would dilute the nSCS waters
46 with the low nutrient North Pacific waters (Farris and Wimbush. 1996), which appeared
47 to be much weaker during April-September (Centurioni et al., 2004). Contribution of
48 nitrogen fixation to new production of the nSCS was generally negligible compared to the
49 nitrate-based new production (Chen et al., 2005; Bombar et al., 2010). Atmospheric
50 deposition of anthropogenic nitrogen could support up to ~20% of the annual new
51 production in the nSCS exceeding those from riverine inputs (Kim et al., 2014). But its
52 contribution would be much less during the spring inter-monsoon season as the reduced
53 rate of atmospheric deposition (Lin et al., 2009).

54 Diapycnal mixing by turbulent dissipation was recently found to be important for the
55 supply of new nitrogen in the nSCS, where the vertical turbulent diffusivities were an
56 order of magnitude higher than the adjacent West Pacific Ocean (Tian et al., 2009; Liu
57 and Lozovatsky 2012; Yang et al., 2014). It was also suggested that phytoplankton
58 blooms off the west coast of the nSCS could be induced by wind stress curl-driven
59 upwelling during the spring inter-monsoon season (Wang and Tang 2014), which would
60 cause a local uplift of isopycnals leading to nutrient injection into the euphotic zone with
61 subsequent changes of community structure and productivity (Rykaczewski and Checkley
62 2008; Li et al., 2015). By modifying the surface wind stress and wind stress curl via
63 air-sea coupling, the eddy-induced Ekman pumping (Gaube et al., 2013) was important
64 for phytoplankton production in the nSCS during the inter-monsoon transition period (Lin
65 et al., 2010). As both intermittent turbulent diffusion and wind-driven Ekman pumping
66 affect the vertical transport of nutrients on temporal scales similar to the generation time

67 of phytoplankton, they will have large influences on plankton dynamics of the upper
68 ocean (Cullen et al., 2002). It is therefore important to investigate the roles of these two
69 mechanisms in driving the variability of phytoplankton biomass and primary production
70 in the large area of the nSCS.

71 Spatial distribution of phytoplankton at sea is a result of complex interactions
72 between physical and biological processes (Davis et al., 1991; Abraham 1998). In
73 addition to the vertical nutrient fluxes, phytoplankton biomass and productivity of the
74 nSCS are influenced by growth-grazing dynamics (Chen 2005; Huang et al., 2011; Zhou
75 et al., 2011; Chen et al., 2013). Shifts in the dominance of phytoplankton species in the
76 western South China Sea were believed to be driven by a close coupling of the mortality
77 rates of different phytoplankton groups via common grazers such as nanoflagellates
78 (Chen et al., 2009). There was on average ~61% of phytoplankton growth lost to
79 microzooplankton grazing in coastal upwelling regions of the nSCS in response to
80 increased nutrient fluxes, whereas growth and grazing mortality rates were mostly
81 balanced on the shelf and shelf break areas without upwelling events (Huang et al., 2011).
82 It was also suggested that the balance of phytoplankton growth and microzooplankton
83 grazing in the pelagic nSCS could be perturbed by physical disturbances such as eddies,
84 fronts, and typhoons, leading to large deviations of planktonic ecosystem from the steady
85 state (Zhou et al., 2011; Chen et al., 2013).

86 Here, we present results of a field survey from the coastal ocean zones to the offshore
87 pelagic zones in the nSCS conducted during the spring inter-monsoon transition of May
88 2014, when the region was characterized by prevailing low nutrient conditions as a result
89 of weak and variable winds (Lin et al., 2010). Comprehensive measurements were made
90 for hydrographic and biogeochemical properties, as well as biological rates including
91 phytoplankton growth and grazing rates and net nutrient consumption rates. We also
92 performed estimations of the vertical turbulent diffusivity and diffusive nutrient fluxes
93 using a Thorpe-scale method (Gargett and Garner 2008; Li et al., 2012) and the upwelling
94 nutrient fluxes by Ekman pumping using satellite-derived wind stress curl (Gill 1982;
95 Risien and Chelton 2008). In synthesizing these field data, the focus of this paper are to
96 (1) investigate the spatial patterns of vertical nutrient fluxes in the nSCS, (2) determine
97 the relative roles of turbulent diffusion and Ekman pumping to vertical transport of

98 nutrients in the upper ocean, and (3) understand the linkage between vertical nutrient
99 fluxes and phytoplankton dynamics in the nSCS during the spring inter-monsoon period.

100

101 **2. Materials and methods**

102 2.1. Site description, field sampling, and measurements

103 There are typically high nutrients in the coastal regions of the nSCS due to river
104 discharge, inter-shelf transport, and upwelling and mixing (Gan et al., 2010), in contrast
105 to the oligotrophic low-latitude offshore regions with strong stratification. The nSCS is
106 also strongly influenced by Kuroshio intrusion through the Luzon Strait (Farris and
107 Wimbush 1996). The intruded Kuroshio waters with higher temperature and salinity but
108 lower nutrients are often transported westward via eddies and Ekman advection
109 (Centurioni et al., 2004) influencing the large area of the nSCS on seasonal time-scales.

110 A field survey of the nSCS (Fig. 1) was conducted during May 2014 aboard the *R/V*
111 *Shiyan III* of the South China Sea Institute of Oceanology. From May 14th to May 16th,
112 2014, a transect from the coastal waters near Shantou to the offshore waters near the
113 Luzon Strait was comprehensively sampled to investigate the spatial patterns of
114 hydrographic and biogeochemical properties of the nSCS. Station S₁ (22°N, 119.5°E) was
115 chosen as a reference time-series station with continuous CTD sampling of 13 casts
116 within 24 hours (start: 10:00 am, May 18th, 2014). Stations A (21.9°N, 120°E with a
117 bottom depth of 1547 m) near the southwest of Taiwan and station B (20.5°N, 117°E with
118 a bottom depth of 607 m) in the southeast of Dongsha Islands were selected for dilution
119 experiments to quantify phytoplankton growth and microzooplankton grazing rates.

120 Discrete seawater samples at depths of 0 m, 25 m, 50 m, 75 m, 100 m, 200 m, 300 m,
121 500 m, and 700 m were collected using a SeaBird SBE 9/11 CTD rosette water sampler
122 system, providing high resolution hydrographic measurements of the upper water column
123 with internal pressure, conductivity, and temperature sensors. We define euphotic zone as
124 the layer above 1% of surface Photosynthetically Active Radiation (PAR), measured by a
125 PAR sensor (QSP200L, Biospherical Instrument, Inc.). After inline filtrations from the
126 PVC Niskin bottles through 0.8 µm Nuclepore filters, seawater samples for nutrients
127 were frozen immediately and stored in a refrigerator until final analyses after the cruise.
128 For chlorophyll-*a* sampling, 500 ml of seawater was gently filtered (<50 mmHg) through

129 a GF/F (Whatman) filter, which was wrapped in a piece of aluminum foil and kept at
130 -20°C on board. Upon return to the lab, chlorophyll-*a* samples were sonicated for 20 min
131 and extracted in 5 ml 90% acetone at 4°C in the dark for 24 hours. These samples were
132 centrifuged at 4000 rpm for 10 min before final determinations by standard fluorescence
133 methods (Parsons et al., 1984) using a Turner Designs Model 10 Fluorometer.
134 Concentrations of nitrate plus nitrite, phosphate and silicate were determined by a Seal
135 AA3 auto analyzer (Bran-Luebbe, GmbH). The low concentrations of nitrate plus nitrite
136 and phosphate within the euphotic zone were also determined by the long-cell method (Li
137 et al., 2008; Li and Hansell 2008) by incorporating a 50 cm liquid waveguide cell to AA3
138 with detection limits of $\sim 0.02\ \mu\text{M}$ and $\sim 0.01\ \mu\text{M}$, respectively.

139

140 2.2. Remote sensing observations

141 High-resolution satellite data, including sea surface temperature (SST), sea surface
142 chlorophyll (SSChl), surface geostrophic velocities, as well as surface wind stresses and
143 Ekman velocities, were used to assess the spatial change of these surface properties in the
144 nSCS during the study period. Monthly averaged sea surface chlorophyll-*a* ($0.04^{\circ}\times 0.04^{\circ}$)
145 was acquired from the NASA's Moderate Resolution Imaging Spectroradiometer data
146 observed by the Aqua Satellite (MODIS-Aqua). Five-day-mean surface velocity fields
147 ($0.3^{\circ}\times 0.3^{\circ}$) were derived from multi-satellite altimeter (TOPEX, JASON-1, ERS-2,
148 ENVISAT and GFO) and scatterometer data distributed by the NOAA's Ocean Surface
149 Current Analysis -Realtime (OSCAR) program, which had been largely validated by a
150 variety of field measurements including global drifts, moorings, and shipboard ADCP.
151 Daily sea surface temperature ($0.1^{\circ}\times 0.1^{\circ}$) was acquired from the NOAA's Geostationary
152 Operational Environmental Satellite –Polar Operational Environmental Satellite program
153 (GOES-POES). Daily Ekman upwelling velocities and surface wind stresses with a
154 resolution of $0.25^{\circ}\times 0.25^{\circ}$ were derived from the Advanced Scatterometer data by the
155 European Meteorological and Operational satellite program (METOP-ASCAT). The
156 Ekman pumping velocity (w_e , negative for downwelling) at the depth of Ekman layer is
157 calculated as (Gill, 1982)

$$158 \quad w_e = \frac{1}{\rho_w} \left(\nabla \times \frac{\tau}{f} \right)$$

159

(1)

160 where ρ_w is the density of seawater, which is assumed constant at 1024 kg m^{-3} ; f is the
161 Coriolis parameter; τ is the vector of wind stress.

162

163 2.3 Thorpe-scale analyses and vertical diffusivity

164 We applied a Thorpe-scale based approach (Thorpe 1977; Galbraith and Kelley 1996;
165 Gargett and Garner 2008; Li et al., 2012) to estimate fine structure and turbulent
166 diffusivity for each station using CTD downcast data. The method combines several
167 criteria to determine the real overturns from a density profile (Li et al., 2012), including
168 the test of minimum thickness, the run-length and water mass tests (Galbraith and Kelley
169 1996), as well as the tests of minimal overturn ratio and maximal T/S tightness (Gargett
170 and Garner 2008). These criteria ensure that the maximal density difference within an
171 overturn is greater than twice the measurement noise (0.001 kg m^{-3}). The length scale of
172 an overturn is larger than twice the vertical resolution (Nyquist theorem) and larger than a
173 minimum thickness (Galbraith and Kelley 1996). The percentage of positive/negative
174 displacements within an overturn (the overturn ratio) is larger than 0.2 and the deviations
175 on a T/S diagram are less than 0.003 (Gargett and Garner 2008). The vertical resolution
176 of CTD sampling during the cruise was $\sim 10 \text{ cm}$ with a fall rate of $\sim 2.4 \text{ m s}^{-1}$. Therefore,
177 only overturns larger than 0.5 m are included, to obtain five data point resolution. We
178 discard data in the upper 10 m , as the Thorpe approach is not strictly valid there. Once an
179 overturn is identified, the Thorpe scale (L_T) is calculated from the root mean square of the
180 vertical displacement (d_z) as $L_T = (\sum d_z^2)^{0.5}$.

181 Turbulent kinetic energy dissipation rate (ε) is calculated from L_T and N by

182

$$\varepsilon = 0.64 \cdot L_T^2 \cdot N^3$$

183

(2)

184 where N is the buoyancy frequency given by $N^2 = -g\rho_0^{-1}(\partial\rho/\partial z)$ with g the gravitational
185 acceleration, ρ_0 the mean density, and $\partial\rho/\partial z$ the density gradient across each overturn
186 (Galbraith and Kelley 1996). According to Osborn (1980), the vertical diffusivity (K_z) can
187 be estimated from ε and N by

188

$$K_z = 0.2 \cdot \varepsilon \cdot N^{-2}$$

189

(3)

190 The diffusive nutrient fluxes at the depth of interest can be estimated by multiplying the
191 diffusivity (K_z) by the local nutrient gradient ($\partial C/\partial z$). Nutrient gradient, at the depth of Z_i
192 with the concentration of C_i , is approximately estimated by $(C_{i+1}-C_i)/(Z_{i+1}-Z_i)$, with C_{i+1}
193 the concentrations at Z_{i+1} immediately next to Z_i .

194

195 2.4 Setup of dilution experiments

196 Phytoplankton growth and microzooplankton grazing in the surface waters of stations
197 A and B near the edge of continental shelf were assessed on board using dilution
198 technique (Landry and Hassett 1982; Landry et al., 1998; Li et al., 2011) on May 13th and
199 May 17th, 2014. All the bottles, tubing and carboys were soaked in 10% (v/v)
200 hydrochloric acid solution for over 24 hours and they were rinsed several times with
201 deionized water and seawater before each experiment. Surface seawater, collected by an
202 acid-washed polyethylene bucket, was screened through a 200- μ m mesh before being
203 transferred into polycarbonate carboys as raw seawater. A dilution series was prepared
204 with 0%, 25%, 50%, 75%, and 100% unfiltered seawater in duplicated polycarbonate
205 bottles (0% unfiltered seawater sample was not performed at station B). Measured
206 amounts of particle-free seawater, obtained by filtering the raw seawater with 0.45 μ m
207 filters, were added to 2.4-liter polycarbonate bottles. These samples were then enriched
208 with additional nutrients to promote constant growth of phytoplankton. Finally, each
209 bottle was gently filled with unfiltered seawater to its capacity. There was also one bottle
210 filled with 100% unfiltered raw seawater without nutrient enrichment to serve as the
211 control for our experiment. All the bottles were tightly capped and incubated for 24 hours
212 in a deck incubator, which was covered with a neutral density screen to mimic the natural
213 sunlight and filled with flowing seawater from the sea surface to control the temperature.
214 Duplicate 300 ml samples were taken from each bottle before and after the dilution
215 experiments for chlorophyll-*a* measurements.

216 Specific rates of nutrient-saturated phytoplankton growth (μ_n , d^{-1}) and
217 microzooplankton grazing (g , d^{-1}) are estimated by least-square regression between the
218 net growth rates (η , d^{-1}) and the dilution factors (D) as

219
$$\eta = \frac{1}{t} \ln \left(\frac{P_t}{P_0} \right) = \mu_n - D \cdot g$$

220 (4)

221 where P_0 and P_t are the initial and final concentrations of chlorophyll-*a*, respectively and
 222 t is the duration of the incubation. The natural phytoplankton growth rate (μ), which is
 223 often subjected to nutrient limitation (Landry et al., 1998), is finally estimated from the
 224 net growth rate of raw seawater without nutrient enrichment (η_{raw}) by $\mu = \eta_{\text{raw}} + g$.

225 To examine the response of the phytoplankton community to nutrient enrichment, two
 226 bottles of raw seawater with nutrient additions were incubated for 4 days, with
 227 chlorophyll-*a* and nutrient samples taken at the very beginning and each day afterwards.
 228 Nutrient data within the exponential growth phase is used to estimate the specific net
 229 nutrient consumption rate (m) of the incubated community by linear regression of $\ln(C)$
 230 and t assuming

231
$$\frac{dC}{dt} = -m \cdot C$$

232 (5)

233 where C is the concentration of dissolved nutrients in the sample.

234

235 3. Results

236 3.1 Hydrographic dynamics of the nSCS

237 During the survey of May 2014, waters of the nSCS can be grouped into three regions
 238 (Fig. 1): the coastal ocean zone (stations C₁₋₆), the offshore pelagic zone (stations C₇₋₁₀),
 239 and the water-intrusion zone near the Luzon Strait (stations C₁₁₋₁₃). These three different
 240 zones were influenced by a diverse set of physical processes. The coastal ocean zone,
 241 which can be further separated into two subregions including the nearshore area (stations
 242 C₁₋₂) and the continental shelf (stations C₃₋₆), was strongly affected by wind-driven
 243 upwelling processes including Ekman transport and Ekman pumping (Gan et al., 2010).
 244 The nearshore area was characterized by low sea surface temperature (Fig. 2a) as a result
 245 of upwelling via Ekman transport driven by southwest monsoon along the shore. Ekman
 246 pumping induced by wind stress curl showed a significant increase near the edge of the
 247 continental shelf far away from the coastline (Fig. 2b). Upward transport of the deeper

248 water with lower temperature but higher salinity along the shelf slope was clearly seen
249 during the transect (Fig. 3a and 3b), which could be a result of direct upwelling or
250 alongshore advection of upwelled waters from upstream. Both the offshore pelagic zone
251 and the water-intrusion zone are far from the coast with bottom depths more than 2000 m
252 (Fig. 1). The offshore pelagic zone was relatively stable with weak surface geostrophic
253 currents, while the water-intrusion zone was strongly influenced by Kuroshio intrusion
254 through the Luzon Strait (Fig. 2a).

255 Sea surface temperature from satellite showed a generally increasing trend from the
256 coastal regions near Shantou to the offshore regions near Luzon Strait due to the
257 decreasing latitude (Fig. 2a). The observed cross-shelf gradient of surface temperature
258 from the discrete bottle measurements is in good agreement with the satellite SST data,
259 with an average of 24.0 ± 0.6 °C near the coast, 25.2 ± 0.2 °C on the continental shelf,
260 28.4 ± 0.5 °C in the offshore pelagic zone, and 29.1 ± 0.5 °C near the Luzon Strait (Fig.
261 3a). Surface salinity was less variable than temperature from nearshore to offshore with a
262 difference of less than 0.3 during the survey (Fig. 3b). Although there was slightly higher
263 surface salinity on the continental shelf (34.1 ± 0.1), the average salinity concentration at
264 the surface in the coastal ocean zone (33.9 ± 0.2) was generally the same as those of the
265 offshore pelagic zone (33.8 ± 0.1) and the water-intrusion zone (33.9 ± 0.3). Substantially
266 higher subsurface salinities within the euphotic zone between the offshore pelagic zone
267 and the water-intrusion zone (Fig. 3b) could come from the upwelled Pacific waters
268 southwest of Taiwan (Chao et al., 1996).

269 Directions of wind stresses in the nSCS were generally southwest during the study
270 period except two regions where wind stress changed direction (vectors of Fig. 2b): one
271 in the northwest of Dongsha Islands with southerly winds and the other in the Luzon
272 Strait with westerly winds. There were several places of curl-driven upwelling in the
273 offshore deep-water regions, though the entire area was predominantly downwelling.
274 Large curl-driven upwelling ($>0.5 \times 10^{-5}$ m s⁻¹) was only observed near the edge of the
275 continental shelf over abrupt changes of bathymetry. Strong temporal variations of
276 Ekman pumping velocity (Fig. 2d) could be found in the coastal station of C₆ and the
277 offshore station of C₁₃. Though the vertical velocities by Ekman pumping during our
278 sampling duration of May 14th-16th, 2014 are relatively low, they are representative of the

279 entire spring intermonsoon period from May 8th to June 7th, 2014 with substantially low
280 wind intensity (Fig. 2d).

281

282 3.2 Spatial patterns of chlorophyll-*a* and nutrients in the nSCS

283 Sea surface chlorophyll-*a* in the nSCS during May 2014 was very high in the coastal
284 ocean zone – particularly in the near-shore regions – and decreased slightly on the
285 continental shelf (Fig. 2c). In contrast, there was generally low sea surface chlorophyll-*a*
286 in the large areas of the offshore pelagic zone and the water-intrusion zone.

287 Concentrations of the surface chlorophyll-*a* from discrete measurements during our
288 survey (Fig. 3c), varying from 0.04 to 0.92 $\mu\text{g L}^{-1}$, is in good agreement with the satellite
289 remote sensing data. In particular, surface chlorophyll-*a* along the section shows a
290 general seaward-decreasing trend from the costal regions of $0.72 \pm 0.36 \mu\text{g L}^{-1}$ to the
291 offshore regions of $0.09 \pm 0.04 \mu\text{g L}^{-1}$, which is consistent with the decrease of surface
292 nitrate concentrations from $>1.0 \mu\text{mol L}^{-1}$ near coast to $<1.0 \mu\text{mol L}^{-1}$ in offshore (Fig.
293 3d). There was a surface chlorophyll patch ($\sim 0.3 \mu\text{g L}^{-1}$) found at station C₁₁ between the
294 offshore pelagic zone and the water-intrusion zone during the transect study (Fig. 3c),
295 which could result from a surface phytoplankton bloom spreading from the southwest
296 coast of Taiwan to the offshore regions of the central nSCS (Fig. 2c).

297 Phytoplankton chlorophyll-*a* was vertically well mixed in the coastal ocean zone,
298 with clear subsurface maxima of chlorophyll-*a* only found in the offshore pelagic zone
299 and the water-intrusion zone (Fig. 3c). The depth of the subsurface chlorophyll maxima
300 followed the $\sigma_{\theta} = 23.5$ isopycnal, which became much shallower when approaching the
301 continental shelf from offshore. The vertical distribution of nutrients along the section
302 generally followed the isopycnal surfaces in the upper water column (Fig. 3d-f), revealing
303 the importance of physical control on upper ocean biogeochemistry. The observed uplifts
304 of isopycnals as well as the depths of chlorophyll maximum and nutricline at stations C₆,
305 C₈, C₉, C₁₀, and C₁₂ are consistent with positive upwelling velocities driven by wind
306 stress curl (Fig. 2b). Interestingly, there were substantially higher phosphate and silicate
307 concentrations at depths of ~ 200 m (across the $\sigma_{\theta} = 25.5$ isopycnal) for both stations C₉
308 and C₁₁ in the offshore regions, which could be due to either a horizontal or vertical
309 injection event prior to our survey. Elevated chlorophyll-*a* at station C₁₁ was

310 accompanied by not only the subsurface high nutrients but also the high salinity in the
311 euphotic zone, suggesting possible vertical and horizontal nutrient transports in the upper
312 layer. Curiously, low chlorophyll-*a* was found at station C₉, which showed the highest
313 nutrient concentrations and nutrient gradients. Along the density interval of $\sigma_{\theta} = 25$ and σ_{θ}
314 $= 26$ in the water-intrusion zone there was evidence for isopycnal mixing between the
315 high-nutrient nSCS waters and the adjacent waters of Luzon Strait with lower nutrient but
316 higher temperature/salinity.

317

318 3.3 Vertical diffusivity and diffusive nutrient fluxes

319 Turbulent diffusivity estimated by Thorpe analyses varied substantially from the edge
320 of continental shelf to the west of Luzon Strait during May 2014 (Fig. 4). An overall
321 averaged K_z of $2.5 \times 10^{-4} \text{ m}^2 \text{ s}^{-1}$ for the upper 300 m of the offshore deep-water stations is
322 much higher than the oceanic background diffusivity of $10^{-5} \text{ m}^2 \text{ s}^{-1}$, but is comparable to
323 the previous basin-scale estimates in the nSCS (Tian et al., 2009; Liu and Lozovsky
324 2012). There were relatively high mean diffusivities of 3.6×10^{-4} and $3.3 \times 10^{-4} \text{ m}^2 \text{ s}^{-1}$ at
325 stations C₈ and C₁₁, compared to $2.5 \times 10^{-5} \text{ m}^2 \text{ s}^{-1}$ of station C₉. Although the nitrate
326 gradient at the based of euphotic zone in C₉ (0.12 mmol m^{-2}) was about twice of that in
327 C₁₁ (0.06 mmol m^{-2}), its diffusive nitrate flux ($0.26 \text{ mmol m}^{-2} \text{ d}^{-1}$) was only about 15% of
328 that in C₁₁. Our data reveals a general decreasing of mean diffusivity from $1.1 \times 10^{-3} \text{ m}^2 \text{ s}^{-1}$
329 of C₅ on the continental shelf, to $6.3 \times 10^{-4} \text{ m}^2 \text{ s}^{-1}$ of C₆ over the continental slope, and to
330 $9.1 \times 10^{-5} \text{ m}^2 \text{ s}^{-1}$ of C₇ in the offshore pelagic zone. Yang et al. (2014) measured turbulent
331 diffusivity along a short section near the edge of the continental shelf southwest of
332 Taiwan using a microstructure profiler during May 2004 – about the same place as our
333 stations C₅ to C₇ (Fig. 1). Their results showed high turbulent mixing over the continental
334 shelf with a mean diffusivity of $1.6 \times 10^{-3} \text{ m}^2 \text{ s}^{-1}$ but a much lower diffusivity of 5.2×10^{-4}
335 $\text{m}^2 \text{ s}^{-1}$ over the slope (Yang et al., 2014), which are well comparable with our estimates
336 using Thorpe analyses.

337 Due to intermittent nature of the turbulence dissipation, the vertical structures of
338 diffusivity observed during our study were quite patchy (Fig. 4). In order to investigate
339 the vertical patterns of turbulent diffusivity, we compared the observations of the two
340 incubation stations (stations A and B) with that of the reference time-series station S₁ (Fig.

341 5), which had a better vertical resolution of diffusivity. It is not surprising to find that the
342 diffusivity profile of station A is quite similar to that of station S₁ (Fig. 5), as the two
343 stations are very close to each other (Fig. 1). However, there are substantially higher
344 diffusivities found in station B than in station S₁ (Fig. 5). The average diffusivity at 100 m
345 during our study was about $1.6 \times 10^{-4} \text{ m}^2 \text{ s}^{-1}$ in station A but about $4.4 \times 10^{-4} \text{ m}^2 \text{ s}^{-1}$ in station
346 B. The corresponding diffusive nitrate fluxes at the base of euphotic zone were thus about
347 $0.65 \text{ mmol m}^{-2} \text{ d}^{-1}$ in station A and $3.03 \text{ mmol m}^{-2} \text{ d}^{-1}$ in station B, given their nitrate
348 gradients of 0.05 and 0.08 mmol m^{-2} at 100 m, respectively (Table 1). Region of the
349 southeast Dongsha Islands near station B has been well documented for its high turbulent
350 mixing because of internal waves (e.g. Lien et al., 2005; Chow et al., 2008). Enhanced
351 vertical mixing by nonlinear internal waves generated at the shelf edge near Dongsha
352 Islands (Lien et al., 2005) would lead to a higher surface chlorophyll-*a* and net primary
353 production than the adjacent areas with less influence of internal waves during the
354 summertime (Pan et al., 2012). The high diffusivity and diffusive nitrate flux at station B
355 may also be contributed by physical dynamics associated with high internal waves found
356 in this region. The frontal zones at the edge of eddies are often places of increased
357 vertical mixing (Klein and Lapeyre 2009; Li et al., 2012), though the eddy-induced
358 vertical fluxes may vary substantially between cyclonic, anticyclonic and mode-water
359 eddies (McGillicuddy et al., 2007).

360

361 3.4 Rates of phytoplankton growth, microzooplankton grazing, and specific nutrient 362 consumption

363 Hydrographic and biogeochemical conditions of the two incubation stations were
364 quite different, with much higher temperature (Fig. 6) and salinity (data not shown) but
365 lower nutrients and nutrient gradients in station A than in station B (Fig. 6). Station A was
366 at the edge of a surface phytoplankton bloom (Fig. 2c) spreading from the southwest
367 coast of Taiwan to the offshore pelagic regions, while station B was near the central nSCS
368 with very low sea surface chlorophyll-*a* ($<0.1 \mu\text{g L}^{-1}$). Except for the surface layer,
369 chlorophyll-*a* concentration of station B was generally much higher than that of station A
370 throughout the water column. There was a clear subsurface chlorophyll maximum of ~ 0.4
371 $\mu\text{g L}^{-1}$ at 50 m for station B (Fig. 6), while double peaks of chlorophyll-*a* were found for

372 station A with a surface maximum of $\sim 0.3 \mu\text{g L}^{-1}$ and a subsurface maximum of $\sim 0.1 \mu\text{g}$
373 L^{-1} at 75 m.

374 Rates of phytoplankton growth and microzooplankton grazing at the surface were
375 substantially different between the two stations. The nutrient-saturated phytoplankton
376 growth rate was 1.24 d^{-1} at station B, which was about three times of that at station A
377 (0.44 d^{-1}). On the other hand, the microzooplankton grazing rate of 0.43 d^{-1} at station A
378 was only slightly lower than the grazing rate of 0.60 d^{-1} at station B (Fig. 7). The natural
379 growth rate of phytoplankton, after correction for the effects of nutrient enrichment as
380 described in section 2.3, was 0.28 d^{-1} at station A, much lower than the rate of 1.18 d^{-1} in
381 station B. The rates measured at station B during May 2014 are comparable with previous
382 estimates of growth rates of 1.03 d^{-1} and grazing rates of 0.62 d^{-1} near Dongsha Islands
383 during July 2009 (Chen et al., 2013). Our results for station A are also in good agreement
384 with those found in the non-upwelling area of the south Taiwan Strait (Huang et al., 2011),
385 which suggested mean rates of $0.4\text{-}0.5 \text{ d}^{-1}$ and $0.3\text{-}0.7 \text{ d}^{-1}$ for phytoplankton growth and
386 microzooplankton grazing during July 2004 and 2005.

387 Incubation experiments in station A revealed an exponential growth of phytoplankton
388 chlorophyll-*a* in response to nutrient addition within the first two days, before reaching a
389 stable growth phase on the third day and a decay phase on the fourth day; the
390 chlorophyll-*a* of the control experiment with raw seawater without nutrient additions
391 quickly decreased as nutrients were consumed in the bottles (Fig. 8a). In contrast,
392 phytoplankton of station B showed no response to nutrient enrichment within the first two
393 days of incubation compared to the control experiment (Fig. 8b). Significant increase of
394 incubated chlorophyll-*a* for station B was only found during the last two days of
395 experiment (Fig. 8b). Nutrient utilization during nutrient-enrichment incubations at these
396 two stations were also quite different, with a much slower specific rate of nutrient
397 consumption at station B (0.46 d^{-1}) than at station A (1.03 d^{-1}). These results suggest that
398 there was stronger nutrient limitation of the phytoplankton community at station A than
399 station B during our cruise.

400

401 **4. Discussion**

402 4. 1 Roles of turbulent mixing and curl-driven upwelling on nutrient fluxes of the nSCS

403 during the spring inter-monsoon transition period

404 If the horizontal and atmospheric inputs are ignored, the total nutrient flux into the
405 euphotic zone (J_{total}) is the sum of diffusive flux due to turbulent dissipation ($J_{diff}=K_z\partial C/\partial z$)
406 and the advective flux due to upwelling ($J_{upw}=wC$, negative for downwelling):

$$407 \quad J_{total} = K_z \frac{\partial C}{\partial z} + wC$$

408 (6)

409 To assess the roles of turbulent diffusion and Ekman pumping on vertical transport of
410 nutrients in the nSCS, the diffusive and advective nitrate fluxes at the base of euphotic
411 zone was estimated from the continental shelf to the open sea during May 2014 (see
412 Table 1 for details). Vertical velocity (w) at the based of euphotic zone is assumed equal
413 to the curl-driven upwelling/downwelling velocity (w_e) by Ekman pumping. We have
414 neglected Ekman transport as its effect is restricted only to the near coast (Gan et al.,
415 2010). Variations of w during the transect study is consistent with the isopycnal
416 oscillation along the section (Fig. 3), suggesting the important role of Ekman pumping on
417 physical dynamics of the water column. At the continental slope of station C₆, the vertical
418 nitrate fluxes were largely supported by curl-driven upwelling, with turbulent mixing
419 playing a minor role due to low nitrate gradients. In contrast, the diffusive nitrate flux
420 was over three times of the upwelled nitrate flux at station C₇, immediately adjacent to C₆.
421 Except for station C₁₂, curl-driven downwelling was observed in the deep-water regions
422 during the transect study, leading to downward transport of the low-nutrient surface water
423 to the deeper layer. The upward nitrate fluxes in these stations were thus determined by
424 the intensities of diffusive fluxes working against the downwelling fluxes. There was a
425 negative nitrate flux found at station C₉ where downwelling was stronger than the upward
426 diffusion, resulting in a loss of nitrate from the euphotic zone. Our findings suggest that it
427 is the interplay of turbulent diffusion and curl-driven upwelling/downwelling that
428 controls the vertical fluxes of nutrients into the euphotic zone to support phytoplankton
429 production in the nSCS.

430 For the deep-water stations including the offshore pelagic zone and the water
431 intrusion zone, the integrated chlorophyll-*a* biomass during the transect study shows a
432 positive correlation with the upward nitrate flux ($\int Chl \cdot dz = 16.75 \times J_{total} + 7.7$, $r^2 = 0.58$,

433 $p=0.014$) when stations C₉ is not included (Table 1), supporting the important role of
434 bottom-up control on phytoplankton production in our study area (Chen 2005). From the
435 slope of 16.75, we could estimate a specific new production by vertical nitrate supply of
436 $0.060 \text{ molN (gChl)}^{-1} \text{ d}^{-1}$, which is slightly lower than $0.063\text{-}0.088 \text{ molN (gChl)}^{-1} \text{ d}^{-1}$
437 reported in the nSCS by Chen (2005). Assuming a vertically constant rate of
438 phytoplankton specific growth, a gram chlorophyll-to-carbon ratio of 0.03 and a molar
439 C/N ratio of 6.625, we estimate a vertically integrated primary production of ~ 12.3
440 $\text{mmolN m}^{-2} \text{ d}^{-1}$ in station B and $\sim 1.8 \text{ mmolN m}^{-2} \text{ d}^{-1}$ in station A. The contribution of
441 vertical nutrient fluxes to primary production could thus be $\sim 11\%$ and $\sim 26\%$ in stations B
442 and A, respectively, which are comparable with the f -ratio of $0.14\text{-}0.20$ previously
443 estimated in the nSCS from late March to October (Chen, 2005). In steady status, the net
444 primary production of phytoplankton should be balanced by the upward nutrient flux as
445 well as the downward particle flux. Therefore, a high nutrient flux would correspond to a
446 high net primary production and thus a high biomass accumulation, if other conditions
447 remain the same (species, temperature, light, grazing, etc). Station C₉ is interesting in that
448 the vertical nutrient fluxes are net downward out of euphotic zone, suggesting that the
449 station may not be in steady status. High nutrients here are likely a result of strong
450 horizontal input or a previous diapycnal nutrient injection. In this case, large drawdown
451 of nutrients will be expected by fast growing phytoplankton and by the downward
452 transport of nutrients out of euphotic zone.

453 Uncertainty of the vertical nutrient flux could be contributed by errors in the
454 determinations of vertical diffusivity and vertical velocity, as well as nutrient
455 concentration and gradient. Calculation errors of vertical diffusivity by the Thorpe-scale
456 approach, estimated from the time-series station S₁, were $0.87 \times 10^{-4} \text{ m}^{-2} \text{ s}^{-1}$ at 50 m (n=5),
457 $0.71 \times 10^{-4} \text{ m}^{-2} \text{ s}^{-1}$ at 100 m (n=6), and $0.46 \times 10^{-4} \text{ m}^{-2} \text{ s}^{-1}$ at 150 m (n=7). We therefore
458 obtain an average of $0.68 \times 10^{-4} \text{ m}^{-2} \text{ s}^{-1}$ for the overall uncertainty of diffusivity
459 determined in our study. Uncertainty of vertical velocity by Ekman pumping from
460 satellite observations could be approximately determined at each station by their standard
461 deviations over the sampling duration of May 14th-16th, 2014. Measurement errors of
462 nutrients at depths during the field study should be negligible as the concentrations are
463 considerably higher than the detection limits of the analytical methods. We are not able to

464 quantify the uncertainty of nutrient gradient, as we have only one cast for each station
465 with reduced resolution below the euphotic layer. Meanwhile, the nutrient gradient and
466 related diffusive flux that we have calculated at the base of euphotic zone could be
467 interpreted as a mean value between the two adjacent bottle depths (100-200 m). The
468 final uncertainties for the vertical nutrient fluxes are summarized in Table 1, which vary
469 substantially from 0.10 to 0.98 mmol m⁻² d⁻¹ (n=10) for stations in the offshore regions.

470

471 4.2 Impact of growth-grazing dynamics on phytoplankton chlorophyll biomass in the 472 nSCS

473 Distributions of phytoplankton in the ocean are controlled by complex physical and
474 biological interactions. To assess the influence of growth-grazing dynamics on
475 phytoplankton chlorophyll-*a* biomass in the nSCS, two stations with distinct
476 biogeochemical settings and nutrient fluxes were selected for measurements of
477 phytoplankton growth and microzooplankton grazing rates. In addition, the community
478 response to nutrient enrichments at the two stations was assessed by continuous
479 incubations for up to four days. Previous studies indicates that surface phytoplankton
480 community in the southeast Dongsha Islands is dominated by both diatom and
481 picoplankton such as *Prochlorococcus*, while picoplankton with negligible diatoms are
482 found in the non-upwelling area south of the Taiwan Strait during late spring and early
483 summer (Yang 2009; Huang et al., 2011). Our results of substantially high phytoplankton
484 growth rates observed at station B southeast of Dongsha Islands are in agreement with its
485 high nutrient concentrations and nutrient fluxes compared to station A south of Taiwan
486 Strait. When released from the constraints by nutrient limitation, phytoplankton
487 community will be expected to shift from dominance by picoplankton toward a higher
488 relative abundance of larger phytoplankton because of their higher intrinsic capacity for
489 growth (Agawin et al., 2000).

490 Percentage of the primary production consumed by microzooplankton can be
491 estimated by the ratio of microzooplankton grazing over phytoplankton growth (g/μ)
492 (Landry et al., 1998). High g/μ ratios (~ 1.5) at station A suggest an elevated role of the
493 microbial food web in the south Taiwan Strait, promoting nutrient recycling to support
494 further phytoplankton growth. Whereas, the relatively higher microzooplankton grazing

495 rate but lower g/μ ratio at station B may indicate a greater efficiency of carbon export
496 near the Dongsha Islands, as the greater loss of diatoms through sinking or grazing by
497 mesozooplankton in regions with high nutrient supply (Landry et al., 1998). Natural
498 growth of phytoplankton at station B was much higher than its grazing mortality, leading
499 to a large net growth rate (growth minus grazing) of 0.58 d^{-1} , which is consistent with the
500 high integrated chlorophyll biomass in this station. In contrast, a negative net growth rate
501 of -0.15 d^{-1} was found at station A as a result of higher grazing pressure. The specific
502 phosphate consumption rate of 1.03 d^{-1} at station A was about twice of that at station B
503 (0.46 d^{-1}) suggesting a larger nutrient demand at station A. There was actually a faster
504 response of phytoplankton to nutrient enrichment at station A than at station B indicating
505 a stronger nutrient limitation in the south Taiwan Strait. The negative net community
506 growth and the higher nutrient consumption rate at station A are consistent with the
507 spring phytoplankton bloom of the southwest Taiwan observed in the satellite data (Fig.
508 2c) being in its decline phase. Indeed, the area of the phytoplankton bloom decreased
509 substantially within two weeks and was not visible by the middle of June, 2014 (from
510 weekly mean sea surface chlorophyll-*a* data of MODIS Aqua) supporting the important
511 role of grazing activity on phytoplankton distribution in the nSCS.

512 In conclusion, we have conducted a preliminary study on vertical nutrient fluxes and
513 phytoplankton dynamics in the nSCS. Our results suggest that phytoplankton patchiness
514 in the nSCS during the spring inter-monsoon of May 2014 was largely controlled by
515 vertical nutrient fluxes, which were driven by both turbulent diffusion and wind stress
516 curl-driven upwelling. Our results also revealed an increasing role of turbulent diffusion
517 but a decreasing role of curl-driven upwelling on vertical transport of nutrients from the
518 coastal ocean zones to the offshore pelagic zones in the nSCS. Elevated nutrient fluxes
519 observed near the Dongsha Islands were found to support high new production leading to
520 net growth of phytoplankton community, whereas the low nutrient fluxes of the south
521 Taiwan Strait resulted in a negative net community growth leading to decline of a
522 phytoplankton bloom. As the findings presented here is limited by the very narrow area
523 and the very short period of sampling time, future studies may be improved by addressing
524 the variability of vertical nutrient fluxes and its relationship to phytoplankton dynamics
525 on a much longer time scale over a much broader area of the nSCS.

526

527 *Acknowledgements*

528 We are grateful to the captain and crew of the *R/V Shiyan III* for their helps during the
529 field work. We also thank two anonymous reviewers for helpful comments. This work is
530 supported by a startup fund from a National Talent-Recruitment Program and a grant
531 from the Chinese Academy of Sciences' Strategic Pilot Project No.XDA110202014 (to
532 QPL).

533 *References*

- 534 Abraham, E.R.: The generation of plankton patchiness by turbulent stirring, *Nature*, 391,
535 577-580, 1998.
- 536 Agawin, N.S.R., Duarte, C.M., and Agusti, S.: Nutrient and temperature control of the
537 contribution of picoplankton to phytoplankton biomass and production, *Limnol. Oceanogr.*, 45,
538 591-600, 2000.
- 539 Bombar, D., Dippner, J.W., Doan, H.N., Ngoc, L.N., Liskow, I., Loick-Wilde, N., and Voss,
540 M.: Sources of new nitrogen in the Vietnamese upwelling region of the South China Sea, *J.*
541 *Geophys. Res.*, 115, C06018, doi:10.1029/2008JC005154, 2010.
- 542 Centurioni, L.R., Niiler, P.P., and Lee, D.K.: Observations of inflow of Philippine Sea surface
543 water into the South China Sea through the Luzon Strait, *J. Phys. Oceanogr.*, 34, 113-121, 2004.
- 544 Chao, S.Y., Shaw, P.T., and Wu, S.Y.: Deep water ventilation in the South China Sea,
545 *Deep-Sea Res.*, I 43, 445-466, 1996.
- 546 Chen, B., Liu, H., Landry, M.R., Dai, M., Huang, B., and Sun, J.: Close coupling between
547 phytoplankton growth and microzooplankton grazing in the western South China Sea, *Limnol.*
548 *Oceanogr.*, 54, 1084-1097, 2009.
- 549 Chen, B., Zheng, L., Huang, B., Song, S., and Liu, H.: Seasonal and spatial comparisons of
550 phytoplankton growth and mortality rates due to microzooplankton grazing in the northern South
551 China Sea, *Biogeosciences*, 10, 2775-2785, 2013.
- 552 Chen, Y.L.: Spatial and seasonal variations of nitrate-based new production and primary
553 production in the South China Sea, *Deep-Sea Res.*, II, 52, 319-340, 2005
- 554 Chow, C., Hu, J., Centurioni, L.R., and Niiler, P.P.: Mesoscale Dongsha cyclonic eddy in the
555 northern South China Sea by drifter and satellite observations, *J. Geophys. Res.*, 113, C04018,
556 doi:10.1029/2007JC004542, 2008.
- 557 Cullen, J.J., Franks, P.J.S., Karl, D.M., and Longhurst, A.: Physical influences on marine
558 ecosystem dynamics, in: *The sea*, 12, Robinson, A.R., McCarthy, J.J., Rothschild, B.J. (eds), John
559 Wiley & Sons, New York, 297–336, 2002.
- 560 Davis, C.S., Flierl, G.R., Wiebe, P.H., and Franks, P.J.S.: Micropatchiness, turbulence and
561 recruitment in plankton, *J. Mar. Res.*, 43, 109-151, 1991.
- 562 Eppley, R.W., and Peterson, B.J.: Particulate organic matter flux and planktonic new
563 production in the deep ocean, *Nature*, 282, 677-680, 1979.
- 564 Farris, A., and Wimbush, M.: Wind-induced intrusion into the South China Sea, *J. Oceanogr.*,
565 52, 771–784, 1996.
- 566 Galbraith, P.S., and Kelley, D.E.: Identifying Overturns in CTD Profiles, *J. Atmos. Ocean.*

567 Tech., 13, 688–702, 1996.

568 Gan, J., Lu, Z., Dai, M., Cheung, A., Liu, H., and Harrison, P.: Biological response to
569 intensified upwelling and to a river plume in the northeastern South China Sea: A modeling study,
570 J. Geophys. Res., 115, doi: 10.1029/2009jc005569, 2010.

571 Gargett, A. E., and Garner, T.: Determining Thorpe scales from ship-lowered CTD density
572 profiles, J. Atmos. Ocean. Tech., 25, 1657–1670, 2008.

573 Gaube, P., Chelton, D.B., Strutton, P.G., and Behrenfeld, M.J.: Satellite observations of
574 chlorophyll, phytoplankton biomass, and Ekman pumping in nonlinear mesoscale eddies, J.
575 Geophys. Res., 118, 6349-6370, doi:10.1002/2013JC009027, 2013.

576 Gill, A.E. (Eds.): Atmosphere-Ocean Dynamics, International Geophysics Series, 30,
577 Academic Press, London, 1982.

578 Han, A., Dai, M., Gan, J., Kao, S., Zhao, X., Jan, S., Li, Q., Lin, H., Chen, C., Wang, L., Hu,
579 J. Wang, L., and Gong, F.: Inter-shelf nutrient transport from the East China Sea as a major
580 nutrient source supporting winter primary production on the northeaster South China Sea shelf,
581 Biogeosciences, 10, 8159-8170, 2013.

582 Huang, B., Xiang, W., Zeng, X., Chiang, K., Tian, H., Hu, J., Lan, W., and Hong, H.:
583 Phytoplankton growth and microzooplankton grazing in a subtropical coastal upwelling system in
584 the Taiwan Strait, Cont. Shelf Res, 31, 48-56, 2011.

585 Kim, T.K., Lee, K., Duce, R., Liss, P.: Impact of atmospheric nitrogen deposition on
586 phytoplankton productivity in the South China Sea, Geophys. Res. Letters, 41(9), 3156-3162,
587 2013.

588 Klein, P., and Lapeyre, G.: The oceanic vertical pump induced by mesoscale and
589 submesoscale turbulence, Annu. Rev. Mar. Sci., 1, 351-375, 2009.

590 Landry, M.R., Brown, S.L., Campbell, L., Constantinou, J., and Liu, B.: Spatial patterns in
591 phytoplankton growth and microzooplankton grazing in the Arabian Sea during monsoon forcing,
592 Deep-Sea Res., II, 45, 2353-2368, 1998.

593 Landry, M.R., and Hassett, R. P.: Estimating the grazing impact of marine micro-zooplankton,
594 Mar. Biol., 67(3), 283-288, 1982.

595 Li, Q.P., Franks, P.J.S., and Landry, M.R.: Microzooplankton grazing dynamics:
596 parameterizing grazing models with dilution experiment data in the California Current Ecosystem,
597 Mar. Ecol. Prog. Ser., 438, 59-69, 2011.

598 Li, Q.P., Franks, P.J.S., Ohman, M.D., and Landry, M.R.: Enhanced nitrate flux and biological
599 processes in a frontal zone of the California Current System, J. Plankton Res., 34, 790-801, 2012.

600 Li, Q.P., and Hansell, D.A.: Nutrient distribution in baroclinic eddies of the oligotrophic

601 North Atlantic and inferred impacts on biology, *Deep-Sea Res., II*, 55, 1291-1299, 2008.

602 Li, Q.P., Hansell, D.A., and Zhang, J.Z.: Underway monitoring of nanomolar nitrate plus
603 nitrite and phosphate in oligotrophic seawater, *Limnol. Oceanogr. Methods*, 6, 319-326, 2008.

604 Li, Q.P., Wang, Y., Dong, Y., and Gan, J.: Modeling long-term change of planktonic
605 ecosystems in the Northern South China Sea and the upstream Kuroshio Current, *J. Geophys.*
606 *Res.*, 120, doi:10.1002/2014JC010609, 2015

607 Lien, R., Tang, T., Chang, M., and D'Asaro, E.A.: Energy of nonlinear internal waves in the
608 South China Sea, *Geophys. Res. Lett.*, 32, L05615, doi:10.1029/2004GL022012, 2005.

609 Lin, I., Lien, C., Wu, C., Wong, G.T.F., Huang, C., and Chiang, T.: Enhanced primary
610 production in the oligotrophic South China Sea by eddy injection in spring, *Geophys. Res. Letters*,
611 37, L16602, doi:10.1029/2010GL043872, 2010.

612 Lin, I., Wong, G.T.F., Lien, C., Chien, C., Huang, C., and Chen, J.: Aerosol impact on the
613 South China Sea biogeochemistry: an early assessment from remote sensing, *Geophys. Res.*
614 *Letters*, 36, L17605, doi:10.1029/2009GL037484, 2009.

615 Liu, K.K., Chao, S.Y., Shaw, P.T., Gong, G.C., Chen, C.C., and Tang, T.Y.: Monsoon-forced
616 chlorophyll distribution and primary production in the South China Sea: observations and a
617 numerical study, *Deep-Sea Res., I*, 49, 1387-1412, 2002.

618 Liu, X., Furuya, K., Shiozaki, T., Masuda, T., Kodama, T., Sato, M., Kaneko, H., Nagasawa,
619 M., and Yasuda, I.: Variability in nitrogen sources for new production in the vicinity of the shelf
620 edge of the East China Sea in summer, *Cont., Shelf Res.*, 61-62, 23-30, 2013.

621 Liu, Z.Y., and Lozovatsky, I.: Upper pycnocline turbulence in the northern South China Sea,
622 *Chin. Sci. Bull.*, 57(18), 2302-2306, 2012.

623 McGillicuddy, D.J., Anderson, L., Bates, N., Bibby, T., Buesseler, K., Carlson, C., Davis, C.,
624 Ewart, C., Falkowski, P., Goldthwait, S., Hansell, D.A., Jenkins, W.J., Johnson, R., Kosnyrev, V.,
625 Ledwell, J.R., Li, Q.P., Siegel, D.A., and Steinberg, D.K.: Eddy-wind interactions stimulate
626 extraordinary mid-ocean plankton blooms, *Science*, 316, 1021-1026, 2007.

627 Osborn, T.R.: Estimates of the local rate of vertical diffusion from dissipation measurements,
628 *J. Phys. Oceanogr.*, 10(1), 83-89, 1980.

629 Pan, X., Wong, G.T.F., Shiah, F.K., and Ho, T.Y.: Enhancement of biological production by
630 internal waves: observations in the summertime in the northern South China Sea, *J. Oceanogr.*, 68,
631 427-437, 2012.

632 Parsons, T.R., Maita, Y., and Lalli, C.M. (Eds.): A manual of chemical and biological methods
633 for seawater analysis, Pergamum Press, Oxford, 1984.

634 Risien, C.M., and Chelton, D.B.: A global climatology of surface wind and wind stress fields

635 from eight year QuickSCAT scatterometer data, *J. Phys. Oceanogr.*, 38, 2379-2412, 2008.

636 Rykaczewski, R.R., and Checkley, D.M.: Influence of ocean winds on the pelagic ecosystem
637 in upwelling regions, *PNAS*, 105(6), 1065–1970, 2008.

638 Strom, S. L., Macri, E. L., and Olson, M. B.: Microzooplankton grazing in the coastal Gulf of
639 Alaska: Variations in top-down control of phytoplankton, *Limnol. Oceanogr.*, 52, 1480–1494,
640 2007.

641 Tian, J., Yang, Q., and Zhao, W.: Enhanced diapycnal mixing in the South China Sea. *J. Phys.*
642 *Oceanogr.*, 39, 3191-3203, 2009.

643 Thorpe, S.A.: Turbulence and mixing in a Scottish loch, *Phil. Trans. Royal Soc., London A*,
644 286, 125–181, 1977.

645 Wang, J., and Tang, D.: Phytoplankton patchiness during spring intermonsoon in west coast
646 of South China Sea, *Deep-Sea Res.*, II, 101, 120-128, 2014.

647 Yang, Q., Tian, J., Zhao, W., Liang, X., and Zhou, L.: Observations of turbulence on the shelf
648 and slope of northern South China Sea, *Deep-Sea Res.*, I, 87, 43-52, 2014.

649 Yang, Y.H.: Phytoplankton community structure of the northern South China Sea and the
650 Philippine Sea, Master Thesis (in CHN), National Taiwan Normal University, Taiwan, 73 pp.,
651 2009.

652 Zhou, L., Tan, Y., Huang, L., Huang, J., Liu, H., and Lian, X.: Phytoplankton growth and
653 microzooplankton grazing in the continental shelf area of northeastern South China Sea after
654 typhoon Fengshen, *Cont. Shelf Res.*, 31, 1663-1671, 2011.

655 Table 1: Comparisons of integrated chlorophyll-*a* ($\int Chl \cdot dz$), nitrate gradient ($\partial C/\partial z$), nitrate
656 concentration (NO_3), vertical diffusivity (K_z), upwelling velocity (w_e), diffusive nitrate flux
657 (J_{dif}), upwelled nitrate flux (J_{upw}), and total nitrate flux (J_{total}) for transect stations C₆₋₁₂ and
658 incubation stations A and B at ~1% light depth (~100m depth).

Station	$\int Chl \cdot dz$ [mg m ⁻²]	$\partial C/\partial z$ [mmol m ⁻⁴]	NO_3 [mmol m ⁻³]	^a K_z [10 ⁻⁴ m ² s ⁻¹]	^b w_e [10 ⁻⁵ m s ⁻¹]	J_{dif} [mmol m ⁻² d ⁻¹]	^c J_{upw} [mmol m ⁻² d ⁻¹]	J_{total} [mmol m ⁻² d ⁻¹]
C ₆	16.8	0.001	5.01	6.30±0.68	0.28±0.02	0.05±0.01	1.21±0.09	1.27±0.10
C ₇	20.2	0.077	6.42	0.91±0.68	0.03±0.05	0.60±0.45	0.17±0.27	0.77±0.73
C ₈	22.1	0.079	7.47	3.60±0.68	-0.21±0.08	2.44±0.46	-1.36±0.52	1.09±0.98
C ₉	15.4	0.122	9.52	0.25±0.68	-0.12±0.03	0.26±0.72	-0.99±0.25	-0.72±0.96
C ₁₀	21.7	0.082	9.37	3.45±0.68	-0.18±0.03	2.44±0.48	-1.46±0.24	0.99±0.72
C ₁₁	38.7	0.060	2.08	3.30±0.68	-0.27±0.07	1.71±0.35	-0.49±0.13	1.23±0.48
C ₁₂	20.7	0.029	3.93	1.53±0.68	0.05±0.05	0.39±0.17	0.17±0.17	0.56±0.34
C ₁₃	13.2	0.046	1.98	2.26±0.68	-0.27±0.17	0.91±0.27	-0.46±0.29	0.44±0.56
A	15.7	0.047	2.09	1.60±0.68	-0.09±0.04	0.65±0.28	-0.16±0.08	0.49±0.35
B	24.8	0.080	4.82	4.40±0.68	-0.41±0.11	3.03±0.47	-1.71±0.46	1.33±0.93

659

660 ^a uncertainty of K_z from Thorpe analyses is estimated as $0.68 \times 10^{-4} \text{ m}^2 \text{ s}^{-1}$ (see text for detail)

661 ^b w_e are 3-day-mean of May 14th-16th, 2014, except station B that is of May 12th-14th, 2014

662 ^c assuming vertical velocity at the depth of 100m is equal to w_e .

663 Figure 1: Sampling map in the northeastern South China Sea during May 2014. Dash
664 lines show the topography of the study area; solid dots are the stations for a transect study
665 (C_{1-13}) during May 14th-16th, 2014; star is a time-series reference station (S_1); filled
666 squares are two stations where shipboard dilution experiments were performed (A and B).
667 Inserted plot shows the temperature/salinity diagram for the transect with arrows
668 indicating waters from the coastal ocean zone (thick gray lines), the offshore pelagic zone
669 (thick black lines), and the Kuroshio intrusion zone (thin lines).

670

671 Figure 2: Spatial distributions of (a) sea surface temperature, (b) curl-driven upwelling
672 velocity, and (c) sea surface chlorophyll during the survey, together with (d) the
673 time-series of curl-driven upwelling and wind stress at stations C_6 and C_{13} during
674 May-June, 2014. Vectors in panel (a) and panel (b) are surface geostrophic currents and
675 wind stresses, respectively; [geostrophic current is from OSCAR data](#); upwelling velocity
676 and wind stress are from 3-day mean METOP-ASCAT data; sea surface temperature is
677 3-day-mean GOES-POES data; sea surface chlorophyll-*a* is monthly MODIS-Aqua data.

678

679 Figure 3: Vertical distributions of (a) temperature [T], (b) salinity [S], (c) chlorophyll-*a*
680 [$Chl-a$], (d) nitrate [NO_3], (e) silicate [$Si(OH)_4$], and (f) phosphate [PO_4] along the coastal
681 transect of the northern South China Sea. Overlaid white lines in each panel are
682 isopycnals.

683

684 Figure 4: Profiles of Thorpe displacement (d_z), Thorpe scale (L_T), and turbulent
685 diffusivity (K_z) for nine stations ($C_5, C_6, C_7, C_8, C_9, C_{10}, C_{11}, C_{12}, C_{13}$) from the edge of
686 continental shelf to the west of Luzon Strait. Locations of these stations are shown in
687 Figure 1.

688

689 Figure 5: Comparisons of vertical turbulent diffusivities (K_z) between two stations A and
690 B. Black line is the result of the reference station S_1 with continuous CTD sampling up to
691 13 casts; circles are for station A (2 casts) with squares for station B (2 casts).

692

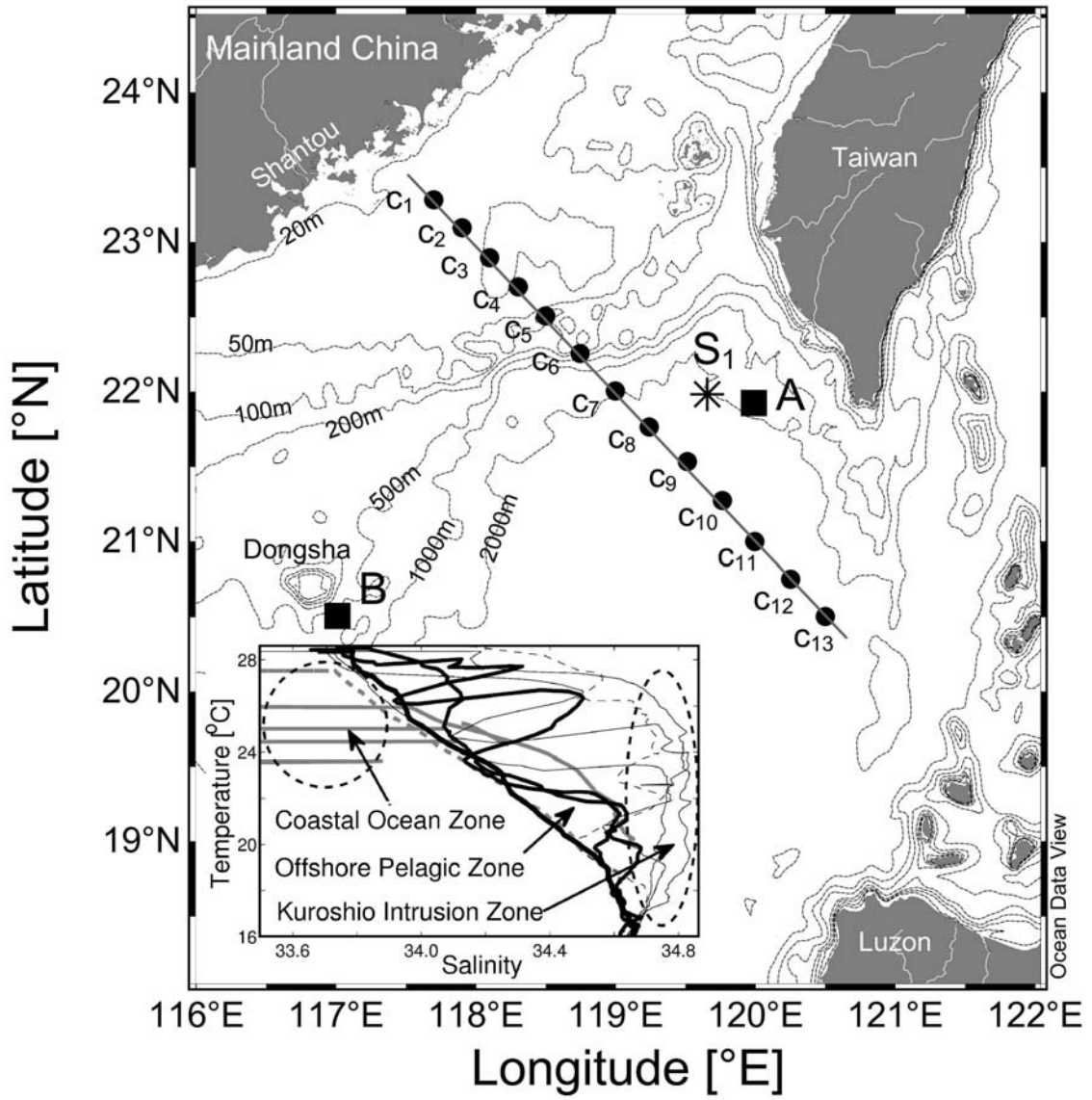
693 Figure 6: Comparisons of vertical profiles of chlorophyll-*a* [$Chl-a$], temperature [T],
694 nutrients [$Si(OH)_4, NO_3, PO_4$], and nutrient gradients between two incubation stations A
695 and B. Thick lines in each panel are for bottom axis with thin lines (open symbols) for top
696 axis; dash lines are for station A with solid lines for station B.

697

698 Figure 7: Dilution experiment plots of phytoplankton net growth rates against the dilution
699 factors for stations A and B. Filled circles are net growth rates of the raw seawater
700 without nutrient enrichments.

701

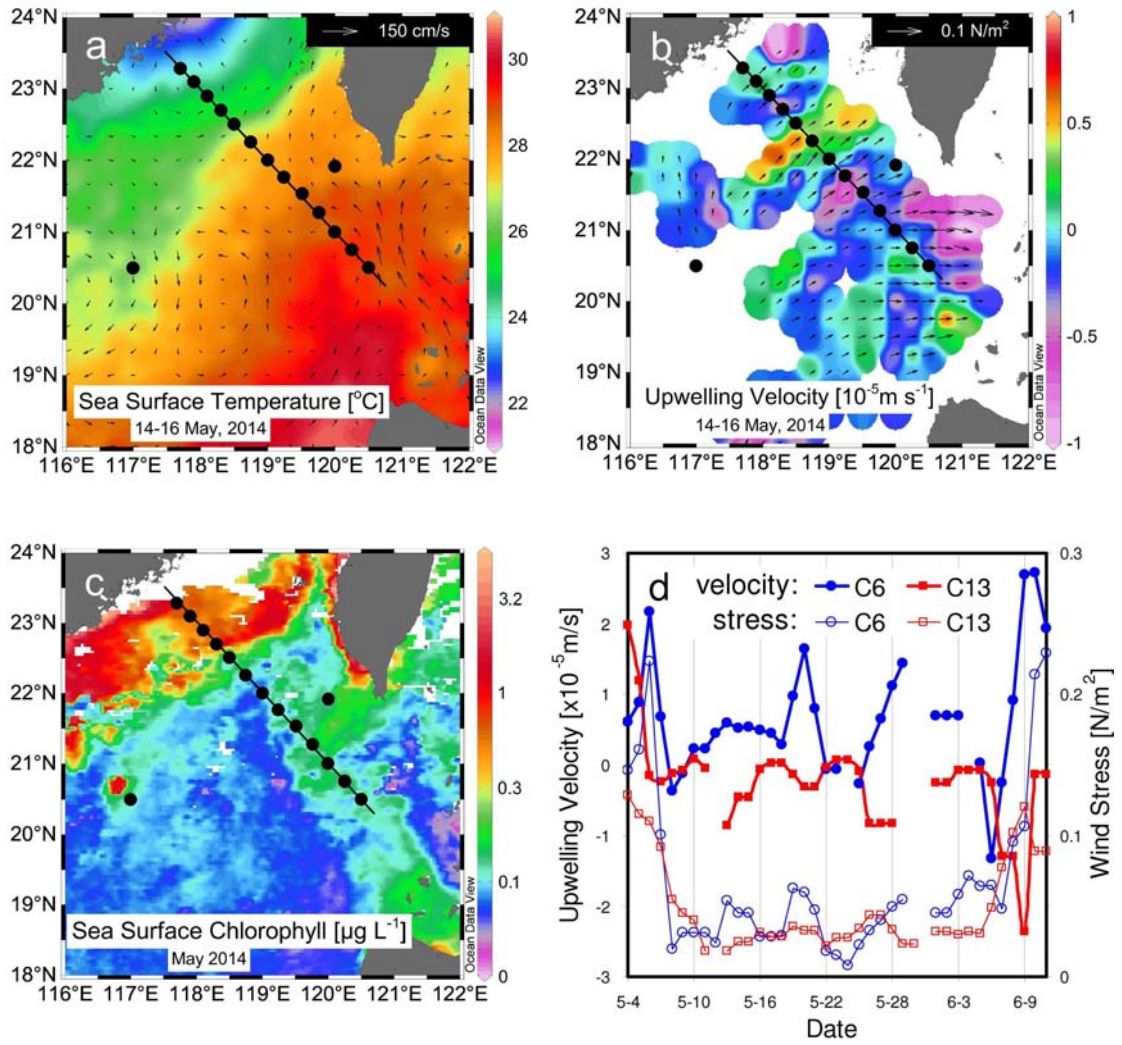
702 Figure 8: Temporal variations of chlorophyll-*a* and phosphate during incubations with
703 and without nutrient enrichments in stations A and B. Dash lines (filled symbols) are for
704 chlorophyll-*a* in left axis with thin lines (open symbols) for phosphate in right axis;
705 control is the incubation of raw seawater without nutrient addition.



706
707
708

Figure 1

709



710
711

Figure 2

712

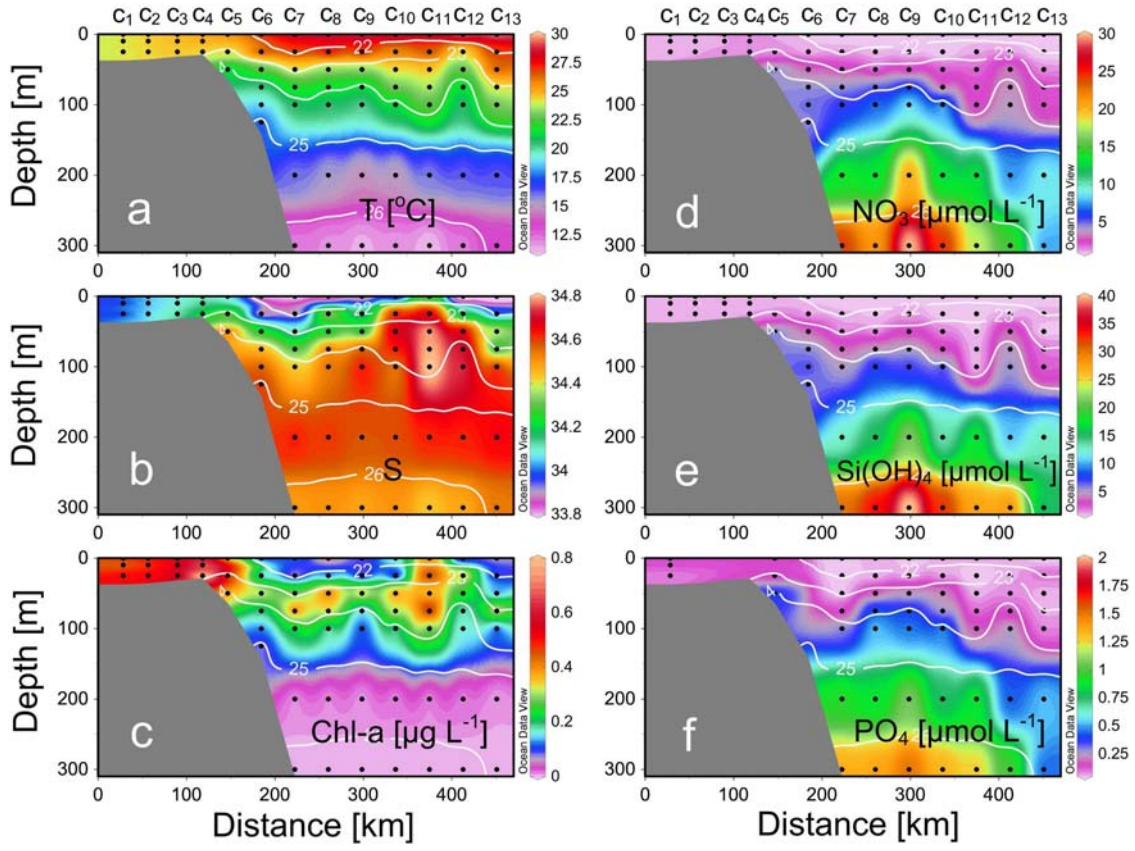


Figure 3

713
714

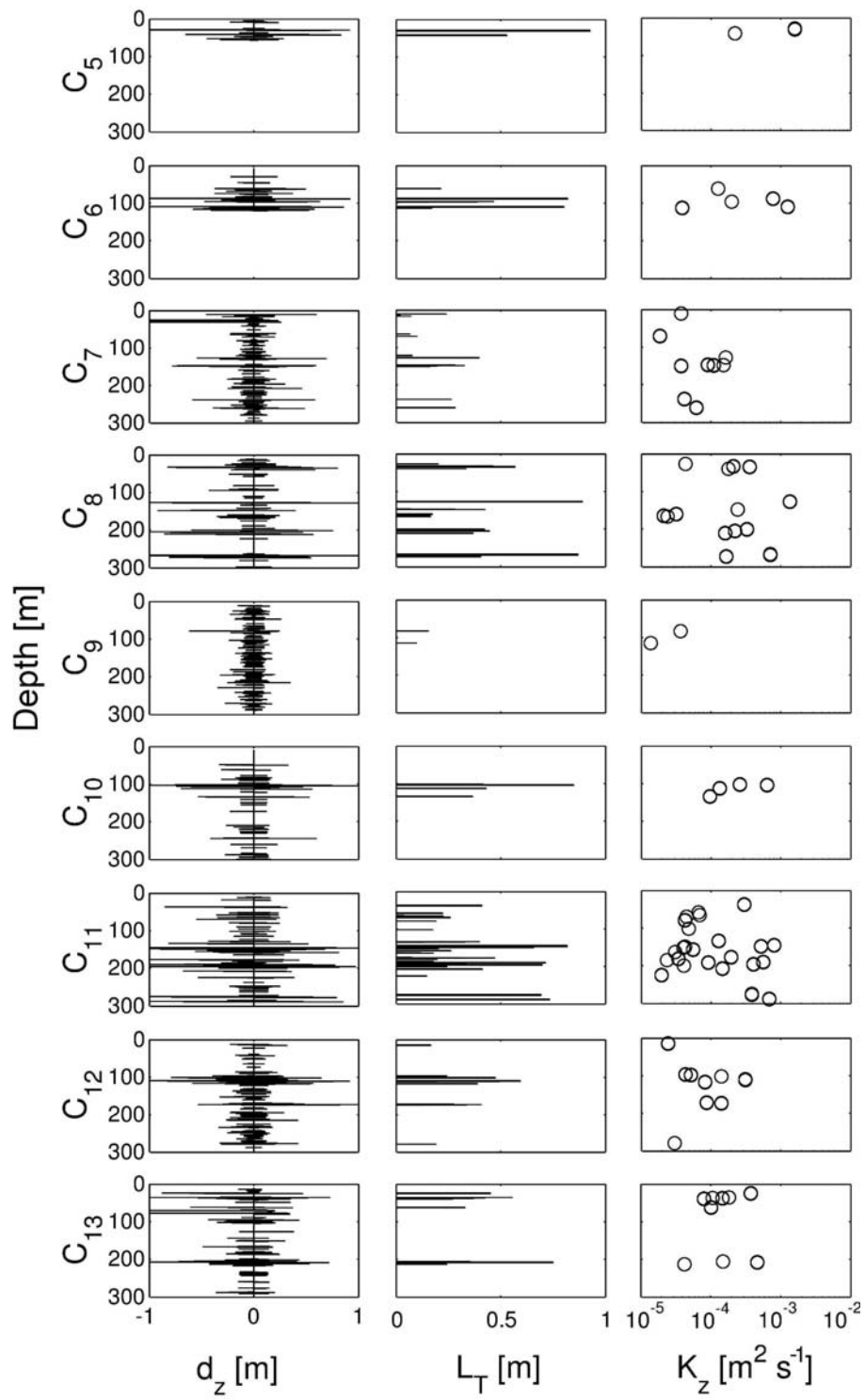
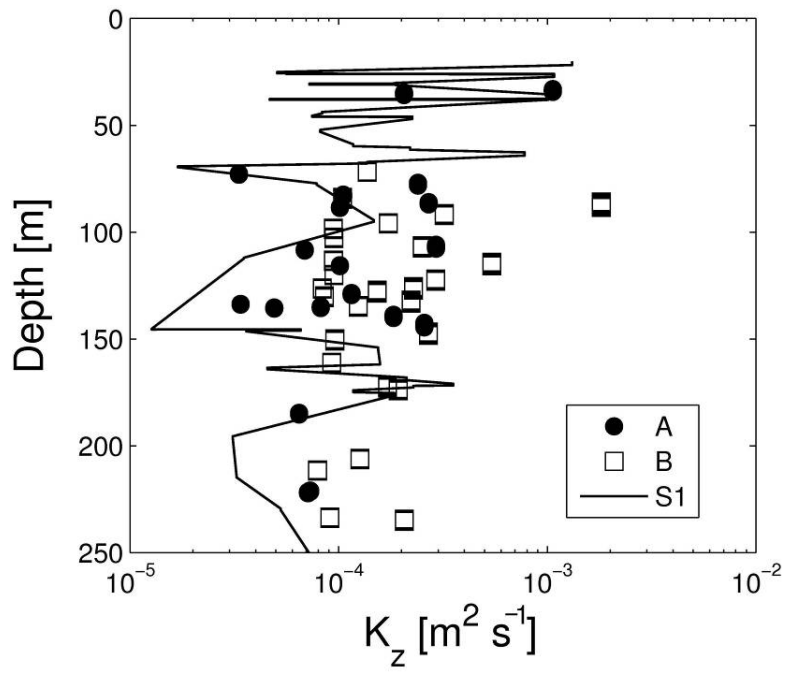


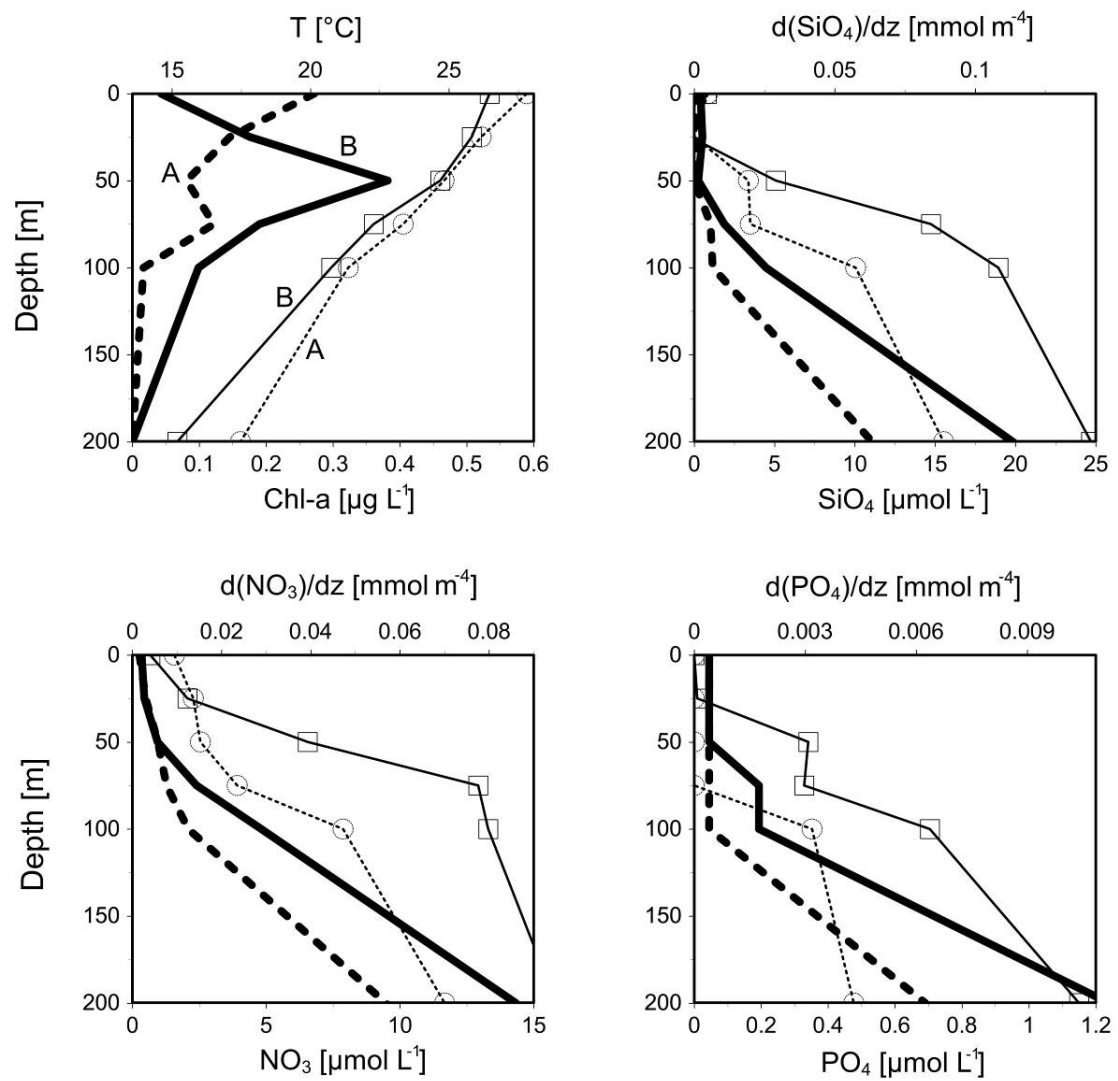
Figure 4

715
716
717



718
 719
 720

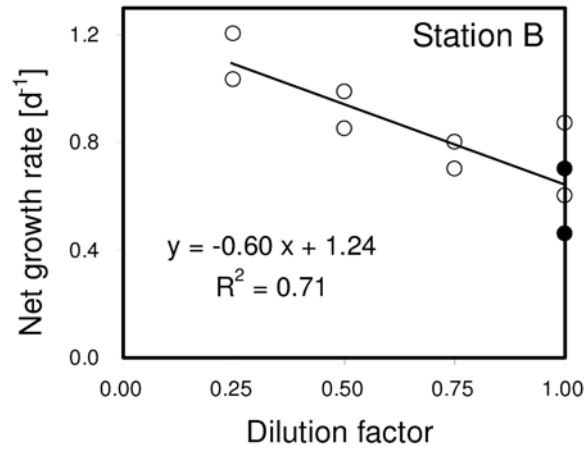
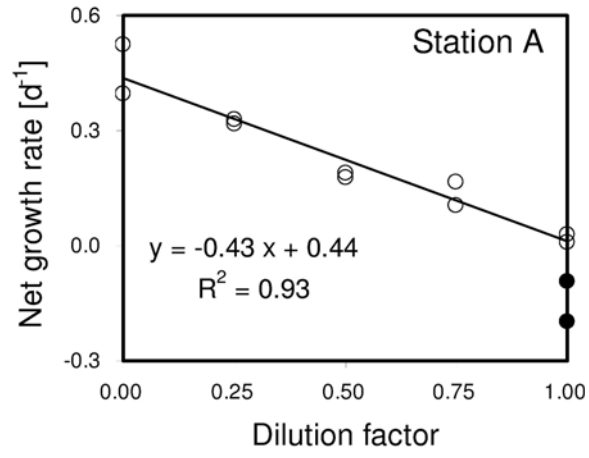
Figure 5



721
722
723

Figure 6

724



725
726
727
728

Figure 7

729

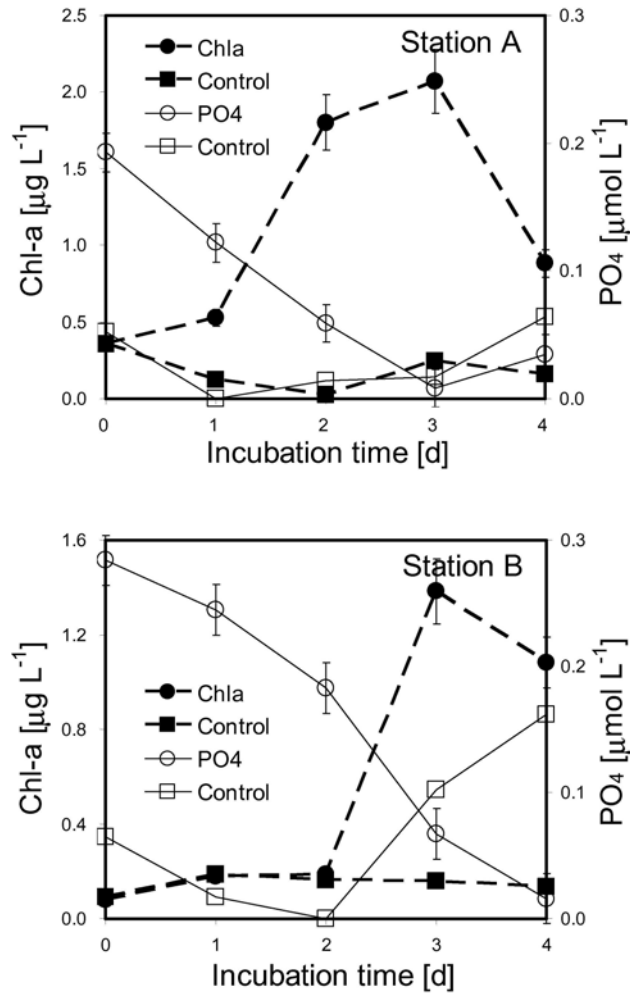


Figure 8

730
731
732
733
734
735